







Article

Synthesis and Investigation of Zeolite TiO₂/Al-ZSM-12 Structure and Properties

Dmitry E. Tsaplin ^{1,2,*}, Vera A. Ostroumova ², Leonid A. Kulikov ¹ , Anna V. Zolotukhina ^{1,2} , Alexey A. Sadovnikov ² , Michail D. Kryuchkov ¹, Sergey V. Egazaryants ¹, Anton L. Maksimov ^{1,2} , Kaige Wang ³, Zhongyang Luo ³  and Evgeny R. Naranov ^{2,*} 

¹ Faculty of Chemistry, Lomonosov Moscow State University, 1 Leninskie Gory Str., Building 3, 119234 Moscow, Russia

² A.V. Topchiev Institute of Petrochemical Synthesis RAS, Leninsky Avenue 29, 119991 Moscow, Russia

³ State Key Laboratory of Clean Energy Utilization, Zhejiang University, Hangzhou 310027, China

* Correspondence: dima-tsaplin-1994@mail.ru (D.E.T.); naranov@ips.ac.ru (E.R.N.); Tel.: +7-495-647-59-27 (ext. 309) (E.R.N.)

Abstract: The textural, structural, morphological, and acidic properties of TiO₂/Al-ZSM-12 zeolite synthesized via the hydrothermal method and using methyltriethylammonium chloride as a template were studied in this study. The structure, size, and shape of the crystallites, and the acidity of the synthesized materials were investigated in detail using the following methods: XRD, low-temperature nitrogen adsorption–desorption, XRF, FTIR, Raman spectroscopy, DRS UV–Vis, DRIFTS, PL, SEM, TEM, solid-state NMR spectroscopy on ²⁷Al, ¹H, ²⁹Si, ¹H-²⁹Si and ²³Na nuclei, NH₃-TPD, TG, DSC, DTA, FTIR-Py, FTIR-2,6-dTBP, FTIR-CD₃CN, and DRIFTS-acid. The presence of tetrahedral titanium in the TiO₂/Al-ZSM-12 zeolite was confirmed by Raman spectroscopy, DRIFT, and ²⁹Si NMR. It was revealed that the crystallites of the TiO₂/Al-ZSM-12 zeolite, elongated along the *b* axis, had a higher acidity compared to the unsubstituted zeolite Al-ZSM-12. The oxidative catalytic activity of the TiO₂/Al-ZSM-12 zeolite was studied in the photoinduced decomposition of the crystal violet dye and it was found that the reaction proceeds most efficiently in the presence of H₂O₂ as an oxidizing agent and TiO₂/Al-ZSM-12 as a catalyst (PCA = 0.157%·min^{−1}).

Keywords: ZSM-12; synthesis; titanium; aluminum; photocatalysis; zeolite



Citation: Tsaplin, D.E.; Ostroumova, V.A.; Kulikov, L.A.; Zolotukhina, A.V.; Sadovnikov, A.A.; Kryuchkov, M.D.; Egazaryants, S.V.; Maksimov, A.L.; Wang, K.; Luo, Z.; et al. Synthesis and Investigation of Zeolite TiO₂/Al-ZSM-12 Structure and Properties. *Catalysts* **2023**, *13*, 216. <https://doi.org/10.3390/catal13020216>

Academic Editor: Antonio Eduardo Palomares

Received: 19 December 2022

Revised: 10 January 2023

Accepted: 12 January 2023

Published: 17 January 2023



Copyright: © 2023 by the authors. Licensee MDPI, Basel, Switzerland. This article is an open access article distributed under the terms and conditions of the Creative Commons Attribution (CC BY) license (<https://creativecommons.org/licenses/by/4.0/>).

1. Introduction

Zeolites are crystalline microporous aluminosilicates, consisting of SiO₄ and AlO₄ tetrahedral fragments, forming a frame structure with a certain pore size, controlled symmetry, and acidity [1,2]. Due to the presence of Al³⁺ in the structure, zeolites exhibit acidic properties, which has led to their widespread use in oil refining and petrochemistry [3–7].

There are a huge number of synthetic zeolites, but only a few of them have commercial applications. Thus, BEA is used in a number of cases of benzene alkylation with propylene [8] and FAU is often found in cracking reactions [9]. However, ZSM-5 zeolite is used in almost all processes due to its three-dimensional system of 10-membered ring pores (10MR) with a size of 5.5 Å × 5.5 Å.

ZSM-12 zeolite (MTW structure type) with a one-dimensional 12-member ring pore system (12-MR) is used as a selective catalyst in refinery reactions, such as aromatic alkylation [10] and disproportionation [11], hydroisomerization of *n*-paraffins [12,13], and hydrocarbon cracking [14].

Zeolite ZSM-12, which is characterized by a one-dimensional system of 12-membered annular pores (12-MR) with dimensions of 5.7 Å × 6.1 Å located in the *b*-direction [15], deserves special mention. However, it should be noted that the resulting diffusion restrictions lead to a decrease in catalytic activity and inefficient use of acid sites in the micropores [13,16].

The catalytic behavior of ZSM-12 zeolites is determined from their textural, structural, and acidic properties, which can be controlled by introducing transition metal ions such as tin [17], gallium [18], vanadium [19], or titanium [20], etc., to improve performance in an industrial catalysis. Thus, Mal et al. [17] synthesized zeolite Sn-ZSM-12 with a Si/Sn > 70 molar ratio using a diquatery ammonium template (1,6-hexamethylene bis(benzyl dimethyl ammonium hydroxide)), which showed efficiency in the oxidation of phenol, *m*-cresol, and *m*-xylene using hydrogen peroxide as an oxidizing agent. Zhi et al. [17] synthesized gallosilicates-MTW-type (Ga/ZSM-12) with a Si/Ga molar ratio of 60 to 120 using methytriethylammonium as a template. The Ga/ZSM-12 zeolite thus obtained exhibited acidic properties similar to those of the Al-ZSM-12 zeolite. In turn, Reddy et al. [19] synthesized a V-ZSM-12 sample with a molar ratio Si/V = 50 and 100 (template 4,4'-trimethylenebis(dimethylpiperidinium) iodide), which was also effective in the oxidation of phenol using hydrogen peroxide as an oxidizing agent.

Due to the close radii of Al (0.53 Å) and Ti (0.56 Å) and similar coordination properties, the latter can serve as a suitable element for the formation of a zeolite frame. The use of titanium oxide TiO₂ and titanium-consisting zeolites in various oxidation reactions to obtain alcohols, aldehydes, and epoxides is widely known [21]. Being a semiconductor, titanium oxide and titanium-consisting zeolites are capable of generating electron-hole pairs under the action of photoradiation, producing active radicals OH• and •O₂⁻ upon interaction with water and oxygen dissolved in the framework [22,23], which greatly speeds up the reaction. This phenomenon is known in the literature as photocatalysis.

The behavior of TiO₂ is the most widely studied due to its high oxidative potential, wide commercial availability, and low toxicity [24,25]. In particular, Labidi and colleagues [26] applied TiO₂ for depolymerization of organosolv lignin (black liquor) using the pulping method in a medium of 1-Butyl-3-methylimidazolium methylsulphate([Bmim][MeSO₄]) ionic liquid. The organosolv liquor treated under UVA irradiation with TiO₂ photocatalyst afforded a considerable yield of phenolic compounds and a 20% oil yield [27]. Au-doped TiO₂ nanoparticles and nanoparticles decorated with β-cyclodextrins demonstrated a high efficiency in the photocatalytic degradation of the methyl orange dye [28].

With regard to titanium-containing zeolites, the [Ti,Al]-β material are active in the oxidation of cyclohexene to epoxy cyclohexane under the action of sunlight using hydrogen peroxide as an oxidizing agent [29]. Analogously, TiO₂/ZSM-5 composites appeared as eco-friendly and efficient adsorbent photocatalysts for dyes removal [30]. Ti-MCM-41 composite, treated with trimethylamine, was using as a cooperative photocatalyst for the selective aerobic oxidation of sulfides illuminated using blue light [31].

Zeolite Ti/ZSM-12 was first synthesized and used as a catalyst for the oxidation of cyclohexane in the presence of hydrogen peroxide by Tuel in 1995 [20], but since then little has been reported about it in the literature.

Due to the fact that post-synthetic processing requires the initial zeolite, and the synthesis under the action of microwave radiation for such a material has not been studied, we chose the hydrothermal (i.e., traditional) method for the synthesis of TiO₂/Al-ZSM-12 zeolite to increase the concentration of acidic Lewis centers. In the future, we plan to synthesize this material with a minimum amount of impurity phases under the influence of microwave radiation.

Thus, the present study is devoted to the thorough investigation of the physical-chemical properties and catalytic behavior of TiO₂/Al-ZSM-12 zeolite, synthesized under hydrothermal conditions for the first time. In particular, we examine the cooperative effect of Ti and Al on the morphology, acidity, and activity in the photocatalytic oxidation of crystal violet dye. This zeolite is used as a catalyst in the photocatalytic reaction of the crystal violet. In industry, it can be used as a catalyst for the isomerization of alkylbenzenes in order to obtain *p*-xylene, a raw material for the synthesis of terephthalic acid.

2. Results

2.1. X-ray Diffraction (XRD)

The X-ray diffraction spectra of the obtained zeolites are presented in Figure 1. The observed reflections are characteristic of zeolite with the MTW structural type [15,32]. It is evident that the introduction of titanium does not affect the structure of this type of zeolite. In $\text{TiO}_2/\text{Al-ZSM-12}$ zeolite, in addition to the main phase, there is a trace amount of impurities: $\text{Al}_2\text{O}_3 \cdot \text{TiO}_2$, $\text{Na}_2\text{O} \cdot \text{TiO}_2$, Silica-X.

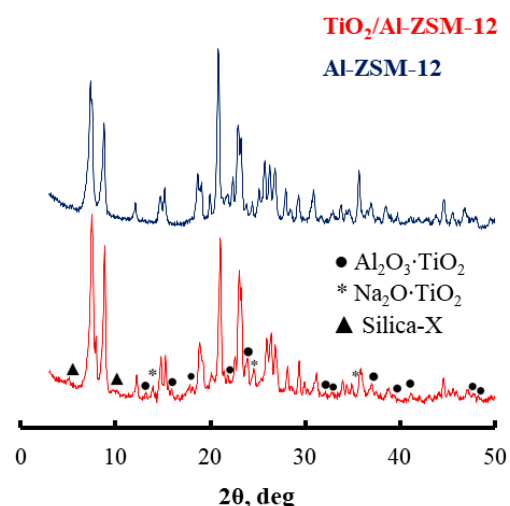


Figure 1. Diffractograms of the synthesized zeolites.

2.2. N_2 Adsorption–Desorption

The area of low pressures ($p/p_0 = 0.05\text{--}0.2$) is characterized using the N_2 absorption method, which indicates the presence of a developed microporous structure in the zeolites (Figure 2). The observed nitrogen adsorption–desorption isotherms belong to type I, characteristic of microporous zeolites with an H4 hysteresis loop [33,34]. The introduction of titanium into the structure somewhat reduces the surface area (Table 1) due to the formation of impurity phases on the surface of the crystallites, which block the access of the nitrogen molecules to the zeolite micropores and thereby reduces the surface area. The decrease in the degree of crystallinity can be affected by the incomplete entry of silicon dioxide into the zeolite framework.

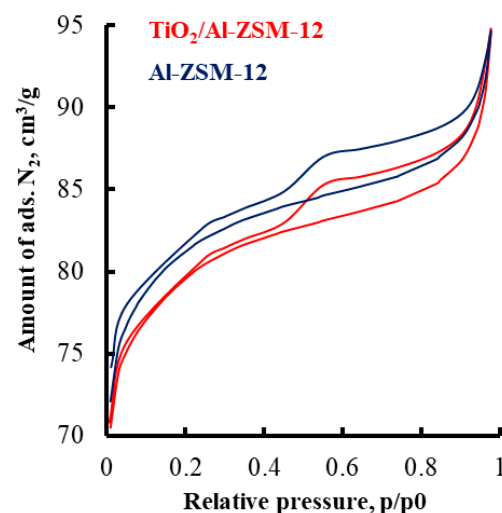


Figure 2. N_2 adsorption–desorption isotherms of synthesized zeolites.

Table 1. Composition and textural characteristics of synthesized zeolites.

Zeolite	$S_{\text{BET}}, \text{m}^2 \cdot \text{g}^{-1}$	$V_{\text{MICRO}}, \text{cm}^3 \cdot \text{g}^{-1}$	$V_{\text{TOTAL}}, \text{cm}^3 \cdot \text{g}^{-1}$	^a Elemental Composition, mol/mol				^b Degree of Crystallinity, %
				Si/Al	Si/Ti	Si/Na	Ti/Al	
TiO ₂ /Al-ZSM-12	266	0.098	0.14	80	384	160	0.2	83
Al-ZSM-12	274	0.1	0.13	105	-	837	-	93

^a Calculated using the XRF method. ^b Calculated using the XRD method.

2.3. Scanning and Transmission Electron Microscopy

According to the SEM data, the crystallites of the Al-ZSM-12 zeolite (Figure 3a) are smaller (5–6 μm) compared to the TiO₂/Al-ZSM-12 zeolite [15]. This is due to the higher Al content in the sample, which affects the rate of nucleation and agglomeration of the particles [35].

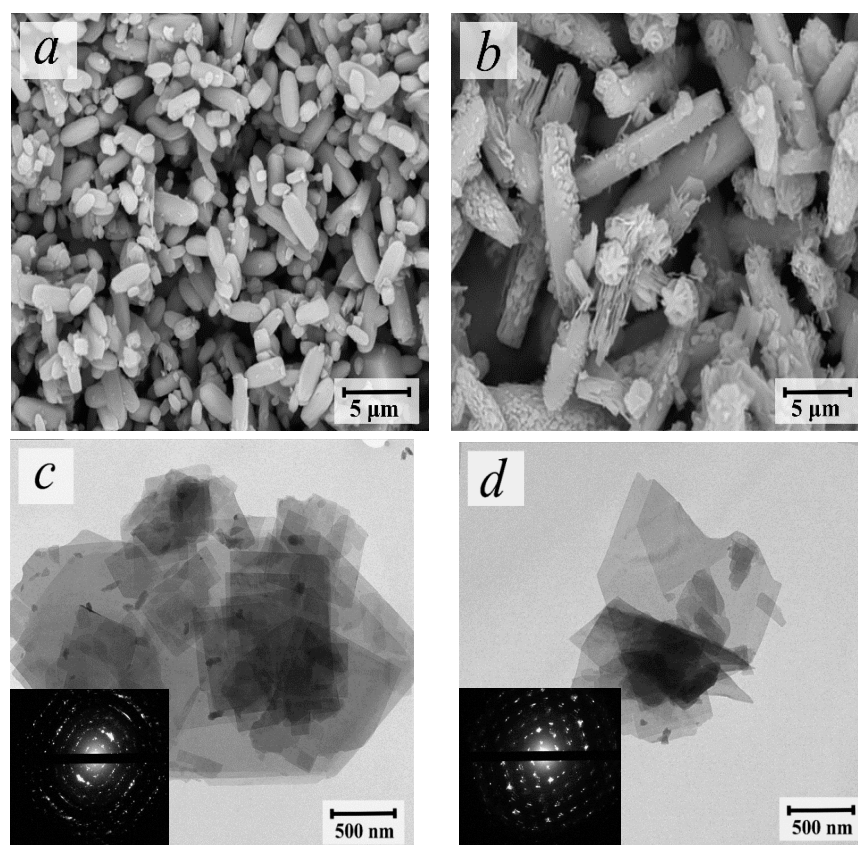


Figure 3. The micrographs of (a,b) SEM- and (c,d) TEM-synthesized zeolites: (a,c)—Al-ZSM-12; (b,d)—TiO₂/Al-ZSM-12 with corresponding SAED patterns.

TiO₂/Al-ZSM-12 zeolite crystallites (Figure 3b) are elongated along the b axis and are characterized by inhomogeneity due to the presence of an amorphous SiO₂ phase or impurity phases (Figure 1) [36]. The Ti ions, which act as a nucleation inhibitor, are present in the material in the form of TiO₄^{2−} anions. As a result, the growth of crystallites along the a and c axes slows down [37].

According to the TEM data, the microporous structures of both zeolites are similar to each other (Figure 3c,d). It can be seen from the electron diffraction patterns that the TiO₂/Al-ZSM-12 zeolite (Figure 3d) is characterized by a hexagonal structure, in contrast to the Al-ZSM-12 zeolite (Figure 3c), which is characterized by a monoclinic structure. Most likely, this is affected not only by the size of the radii of titanium and aluminum (the radius

of the titanium atom is greater than the radius of the aluminum atom), but also by impurity phases that change the parameters of the zeolite crystal lattice:

$$a = 24.9 \text{ \AA}, b = 5.0 \text{ \AA}, c = 24.4 \text{ \AA} \text{—for Al-ZSM-12}$$

$$a = 12.6 \text{ \AA}, b = 11.1 \text{ \AA}, c = 24.4 \text{ \AA} \text{—for TiO}_2/\text{Al-ZSM-12}$$

2.4. Fourier Transform Infrared Spectroscopy (FTIR), Raman Spectroscopy (Raman), UV–Visible Diffuse Reflectance Spectroscopy (DRS UV-Vis), Diffuse Reflectance Infrared Fourier Transform Spectroscopy (DRIFTS), and Photoluminescence Spectroscopy (PL Spectroscopy)

The IR spectra of the obtained materials (Figure 4a) have absorption bands characteristic of zeolites, corresponding to Si–O–Si and Si–O–Al bonds. The absorption bands in the spectra with maxima at 580 and 543 cm^{-1} indicate that in the material there are structures formed by a prism with bases in the form of 12-membered rings, which agrees with the data of [15,38,39]. The absorption band maximum at 515 cm^{-1} most likely corresponds to the Ti–O–Ti bond [40,41].

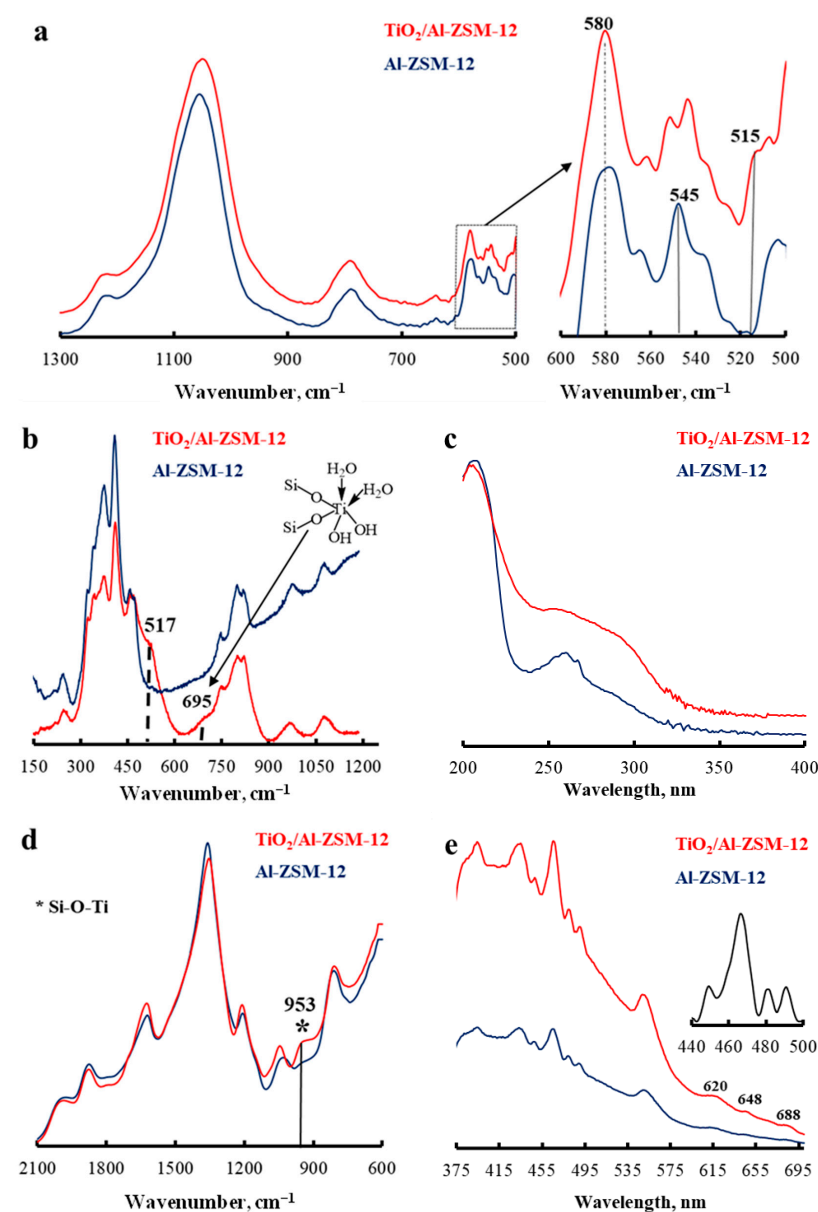


Figure 4. (a) IR-, (b) Raman-, (c) DRS UV-Vis-, (d) DRIFTS-, (e) PL-spectra (insert is lamp emission spectrum) of synthesized zeolites.

The presence of tetrahedral titanium in the $\text{TiO}_2/\text{Al-ZSM-12}$ sample, which forms Si–O–Ti bonds, is confirmed by bands with maxima at 517 cm^{-1} (Raman, Figure 4b) [42,43] and 953 cm^{-1} (DRIFTS, Figure 4d) [44,45]. The Raman spectrum of the $\text{TiO}_2/\text{Al-ZSM-12}$ zeolite also contains a band with the maximum at 695 cm^{-1} , which is responsible for the appearance of octahedral titanium (Figure 4b). A small shoulder in the DRS UV–Vis spectrum (Figure 4c) of the $\text{TiO}_2/\text{Al-ZSM-12}$ zeolite in the region of 250–310 nm indicates the presence of penta- and octa-coordinated titanium [46–48] and the formation of TiO_2 clusters [49].

According to the PL analysis data (Figure 4e), the $\text{TiO}_2/\text{Al-ZSM-12}$ zeolite has wavelengths with maxima at 600–700 nm, which characterize the presence of OH groups and H_2O molecules in the environment of titanium, corresponding to the absorption band maximum at 695 cm^{-1} (Raman, Figure 4b).

2.5. Solid-State Nuclear Magnetic Resonance Spectroscopy (SS NMR) on Different Nuclei

The chemical shift at 55.6 ppm in the ^{27}Al NMR spectra (Figure 5a) indicates the presence of tetrahedral aluminum in the structure of both zeolites [33]. The spectrum of zeolite Al-ZSM-12 contains a chemical shift of about 0 ppm, which is typical for octahedral aluminum.

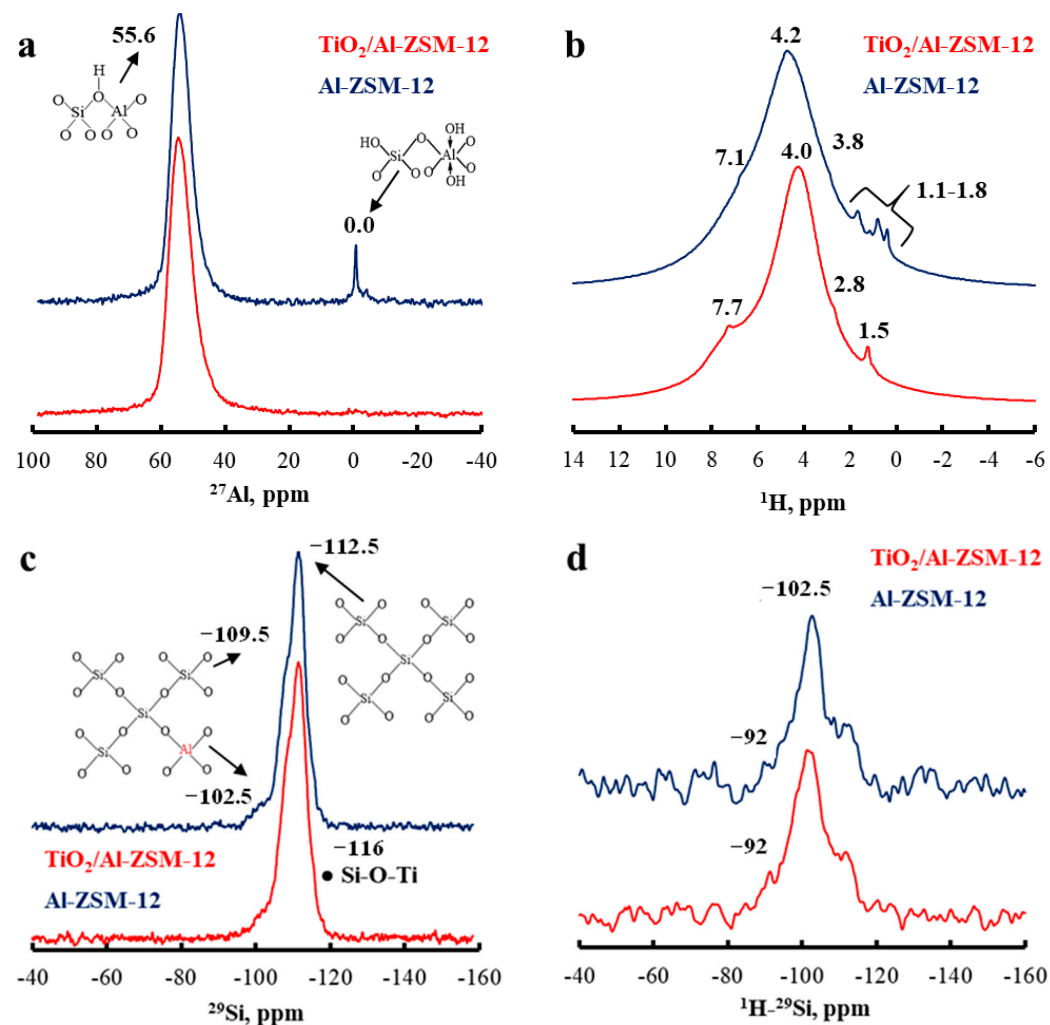


Figure 5. Cont.

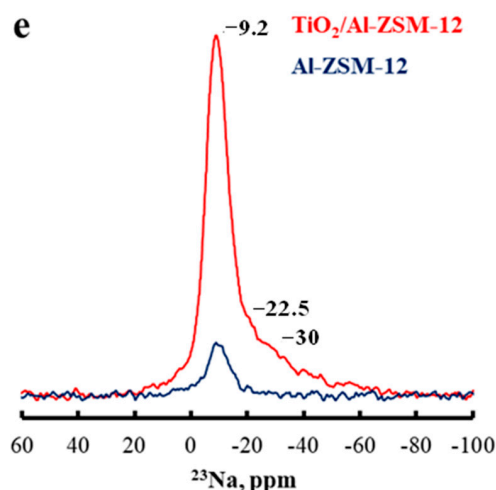


Figure 5. NMR spectra of the solid on (a) ^{27}Al , (b) ^1H , (c) ^{29}Si , (d) ^1H - ^{29}Si CP/MAS, and (e) ^{23}Na nuclei of synthesized zeolites.

The ^1H NMR spectra (Figure 5b) contain isolated Si–OH groups located on the outer surface of the zeolite (1.1–1.8 ppm); internal Al–OH groups (2.8 ppm); fragments of Si–O(H)–Al forming Brønsted acid sites (3.8, 4.0 and 4.2 ppm); hydroxyls associated with Si–OH \cdots O– hydrogen bonds (7.1 and 7.7 ppm). A similar shift for the $\text{TiO}_2/\text{Al-ZSM-12}$ sample at 4 ppm indicates a lower concentration of Brønsted acid sites [50].

Solid ^{29}Si (Figure 5c) and ^1H - ^{29}Si CP/MAS NMR (Figure 5d) were used to study the local binding environment in the synthesized zeolites. The two allowed chemical shifts (at -112.5 and -102.5 ppm) correspond to the Q^4 and Q^3 tetrahedral fragments appearing from the formation of silanol groups on the zeolite surface. The chemical shift at -116 ppm indicates the presence of a Si–O–Ti bond that corresponds to the data from Raman (Figure 4b) and DRIFTS (Figure 4d) [51].

In the ^1H - ^{29}Si CP/MAS NMR spectrum (Figure 5d), the chemical shifts correspond to the same Si states as in the ^{29}Si NMR spectrum (Figure 5c). In the spectra of both samples, a chemical shift is observed at -92 ppm; in the spectrum of the $\text{TiO}_2/\text{Al-ZSM-12}$ zeolite, the intensity of this shift is stronger. Therefore, it can be assumed that the $\text{TiO}_2/\text{Al-ZSM-12}$ zeolite contains a $[\text{Si}(\text{OSi})_2(\text{OAl})_1(\text{OTi})_1]$ particle of the Q^2 type. A similar chemical shift was previously shown in the work of [52] in a study of the Ti-USY zeolite.

The chemical shift at -9.2 ppm in the ^{23}Na NMR spectrum of the $\text{TiO}_2/\text{Al-ZSM-12}$ zeolite (Figure 5e) is more intense due to its higher content of sodium, which corresponds to a lower degree of crystallinity compared to the Al-ZSM-12 zeolite. Moreover, in the spectrum of the $\text{TiO}_2/\text{Al-ZSM-12}$ zeolite, there are two shoulders shifted towards the weak field (-22.5 and -30 ppm), which characterize sodium isolated in 12-membered ring channels very weakly or not subjected to ion exchange [53].

2.6. Thermogravimetric (TG), Differential Scanning Calorimetry (DSC), and Differential Thermal Analysis (DTA)

According to the TG data (Figure 6a), physically adsorbed water is removed in both zeolites up to a temperature of 100°C , which is confirmed by the DSC and DTA data (Figure 6b,c). Thus, the endo- and exothermic peaks in DSC and DTA for the Al-ZSM-12 zeolite are located at 98°C and 88°C , respectively, which indicates not only the removal of adsorbed water during the analysis, but also the complete removal of the template during calcination. The shift of similar peaks to 108°C and 101°C for $\text{TiO}_2/\text{Al-ZSM-12}$ may be due to the removal of occluded water in impurity particles (XRD, Figure 1).

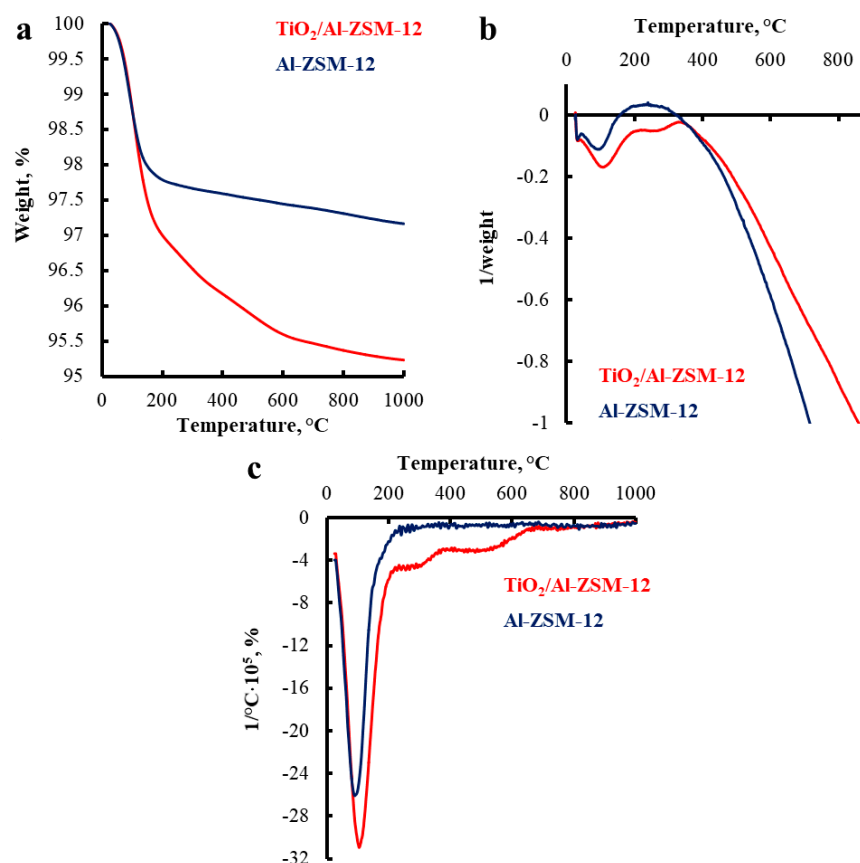


Figure 6. (a) TG, (b) DSC, and (c) DTA of synthesized zeolites.

When the Al-ZSM-12 sample is heated in the temperature range of 130–1000 °C, a gradual decrease in weight loss (2.8%) occurs, which is associated with the destruction of the hydrogen bonds and dehydroxylation of the surface Si–OH and Al–OH groups in the Al-ZSM-12 zeolite. The weight loss for TiO₂/Al-ZSM-12 zeolite is 4.8%. A more intense dehydroxylation in this case indicates a strong interaction of titanium with the OH groups, which is confirmed by the data of Raman (Figure 4b) and PL spectroscopy (Figure 4c) [54].

The acidity of the zeolites was studied using the methods of NH₃-TPD and IR spectra of Al-ZSM-12 and TiO₂/Al-ZSM-12 zeolites with adsorbed probe molecules of pyridine, 2,6-di-tert-butyl-pyridine, deuterated acetonitrile, and DRIFTS-acid, the data of which are shown in Figures 7 and 8 and in Tables 2 and 3.

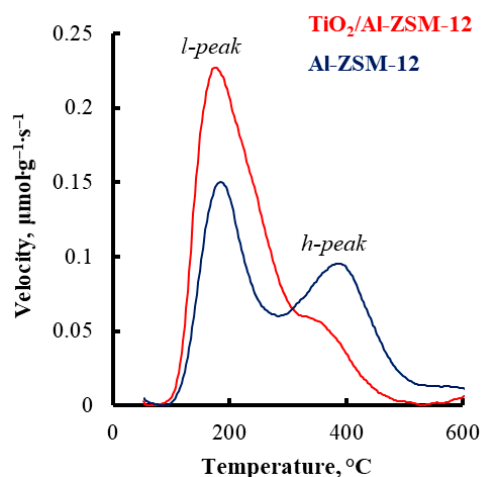
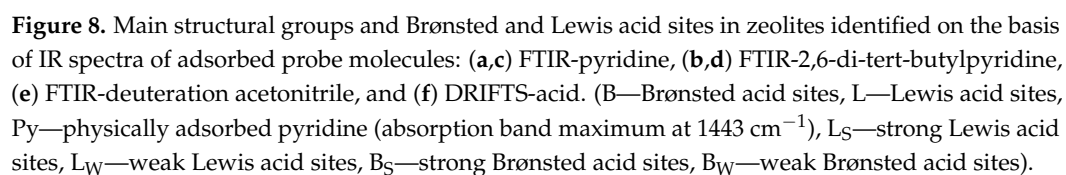


Figure 7. NH₃-TPD synthesized zeolites.



Zeolite	The Number of Acid Sites														
	$\mu\text{mol}_{\text{PYRIDINE}} \cdot \text{g}_{\text{ZEOLITE}}^{-1}$				DRIFTS-Acid, %			$\mu\text{mol}_{2,6\text{-dTBP}} \cdot \text{g}_{\text{ZEOLITE}}^{-1}$				$\mu\text{mol}_{\text{NH}_3} \cdot \text{g}_{\text{ZEOLITE}}^{-1}$			
	LASs	BASs	Total	B/L	BASs			Total	BASs	Weak Sites (100–300 °C)		Strong Sites (300–500 °C)		Total	$\frac{C_{\text{WEAK}}}{C_{\text{STRONG}}}$
					Weak	Medium	Strong			^a LT, °C	Amount	^b HT, °C	Amount		
TiO ₂ /Al-ZSM-12	38	15	53	0.4	83.1	3.2	13.7	100	2.5	188	205	393	32	237	6.41
Al-ZSM-12	5	40	45	8	30.8	8.8	60.4	100	3.1	183	80	363	117	197	0.68

^a LT—Low-Temperature. ^b HT—High-Temperature. LASs—Lewis acid sites. BASs—Brønsted acid sites.

Table 3. Bands identifying the main structural groups of zeolites and Brønsted and Lewis acid sites.

Adsorption Centers of Probe Molecules	Wave Number, cm ^{−1}			
	FTIR-Py	FTIR-2,6-dTBP	FTIR-CD ₃ CN	DRIFTS-Acid
isolated Si–OH groups located on the outer surface of the zeolite	3745	3743	N.D.	N.D.
internal Si–OH	3740–3710		N.D.	N.D.
extra framework Al–OH groups	3665 (Al-ZSM-12)		N.D.	N.D.
Si–O(H)–Al, Brønsted acid sites	3615 and 1547	3608 and 1620	2277 (Al-ZSM-12)	3723 (B _W)
				3674 (B _M)
				3596 (B _S)
silanol nests, (Si–OH) _n	3520	N.D.	2266 (TiO ₂ /Al-ZSM-12)	N.D.
Lewis acid sites, [AlO ₄] [−]	1455	N.D.	2330 (Al-ZSM-12);	N.D.
			2325 (TiO ₂ /Al-ZSM-12)	

N.D.—not identified.

2.7. Temperature-Programmed Ammonia Desorption (NH₃-TPD)

For both samples, the NH₃-TPD data showed the presence of both strong and weak acid sites, displayed by the l- or h-peak, respectively (Figure 7, Table 2). It is evident that, on the one hand, the TiO₂/Al-ZSM-12 sample, compared to Al-ZSM-12, is characterized by a higher concentration of weak acid sites (ammonia adsorption at 100–300 °C) formed by Si–O–Ti fragments and Si–O–Al. The reduced concentration of strong acid sites (ammonia desorption at 300–550 °C), on the other hand, may be caused by incomplete H⁺-Na⁺ ion exchange inside the 12-membered ring channels, which is confirmed by the ²³Na NMR data (Figure 5e).

2.8. Fourier Transform Infrared Spectroscopy of Adsorbed Pyridine (FTIR-Py), 2,6-di-Tert-Butyl-Pyridine at External Surface (FTIR-2,6-dTBP), Deuterated Acetonitrile (FTIR-CD₃CN), and Investigation of Acidity Method Diffuse Reflectance Infrared Fourier Transform Spectroscopy (DRIFTS-Acid)

The IR spectra of the zeolites with adsorbed probe molecules are shown in Figure 8 and in Table 3.

It is evident that in the TiO₂/Al-ZSM-12 zeolite (Figure 8a,b), the intensity of the bands of the silanol and Al–OH groups is inferior to that of the Al-ZSM-12 zeolite due to the isomorphic substitution of aluminum by titanium [48]. Pyridine bonded to the OH groups on the surface of the titanium clusters (Figure 8c) is identified by a band with the absorption maximum at 1575 cm^{−1}, which corresponds to Lewis acid sites [55]. In the TiO₂/Al-ZSM-12 zeolite, the band with the absorption maximum at 1446 cm^{−1} is supposed to indicate an insignificant proportion of tetrahedral titanium, which is also confirmed by the data from Raman (Figure 4b) and DRIFTS (Figure 4d) [56].

It should be noted that for both zeolites, there was not observed any absorption band of adsorbed 2,6-dTBP in the range of 1470–1445 cm^{−1} in the IR spectra (Figure 8d) associated with the Lewis acid sites, which may be explained by the influence of the screening effect of the bulky tert-butyl groups of 2,6-dTBP [57].

According to the adsorption spectra of deuterated acetonitrile (Figure 8e), in zeolites Al-ZSM-12 and TiO₂/Al-ZSM-12, Lewis and Brønsted acid sites were determined, which appear on titanium and aluminum. The concentration of weak Lewis acid sites was determined from the bands with the absorption maximum at 2306 cm^{−1} (Al-ZSM-12) formed by Al³⁺ and at 2300 cm^{−1} (TiO₂/Al-ZSM-12) formed by Ti⁴⁺. The interaction of CD₃CN with the weaker Brønsted acid sites formed by Ti–OH is determined by the band with the absorption maximum at 2284 cm^{−1}.

According to DRIFTS-acid (Figure 8f), the band with the absorption maximum at 3560–3500 cm^{−1} in the spectrum of the TiO₂/Al-ZSM-12 zeolite broadens at the association with H₂O: the more the maximum is shifted to long wavelengths, the stronger the

association (with one or two water molecules). O–H stretch vibrations in the composition of the hydronium cation (H_3O^+) produce bands with the absorption maximum below 3300 cm^{-1} . The DRIFTS-acid data allow the conclusion that the introduction of titanium leads to the redistribution of the number of Brønsted acid sites between the weak and medium sites (Table 3), which agrees with the NH_3 -TPD data. In particular, the number of weak acid sites increases from 30.8 to 83.1%, while the number of medium acid sites decreases from 8.8 to 3.2%.

2.9. Catalytic Tests

The catalytic activity of the synthesized $\text{TiO}_2/\text{Al-ZSM-12}$ zeolite was studied in the oxidation reaction of the crystal violet dye in the light using H_2O_2 as the oxidizing agent. The results are presented in Figure 9 and in Table 4.

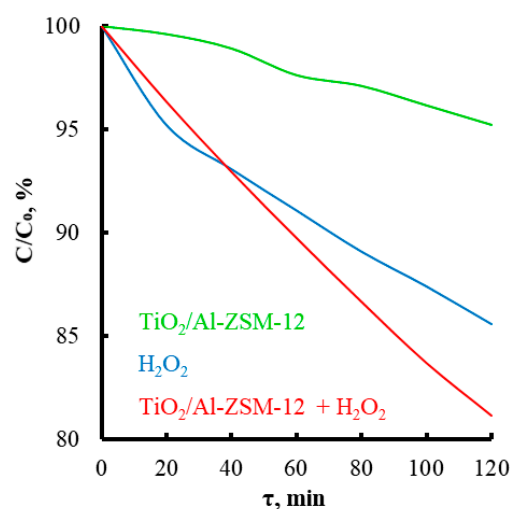


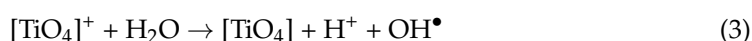
Figure 9. The comparison of the photocatalytic decomposition rate of the crystal violet dye in the presence and absence of hydrogen peroxide.

Table 4. Measured dye concentration in photocatalytic and control experiments.

	$\text{TiO}_2/\text{Al-ZSM-12}$	H_2O_2	$\text{TiO}_2/\text{Al-ZSM-12} + \text{H}_2\text{O}_2$
^a PCA, $\% \cdot \text{min}^{-1}$	0.041	0.112	0.157

^a PCA—photocatalytic activity.

A slight drop in the substrate concentration in the presence of the $\text{TiO}_2/\text{Al-ZSM-12}$ zeolite, but in the absence of H_2O_2 , can be explained by decomposition under the action of atmospheric oxygen catalyzed by Ti^{4+} . The oxidation in this case occurs due to the ability of titanium-containing oxides to generate electron–hole pairs in the valence band under the action of photoradiation (Equations (1)–(3)) [22,23,58–61]. Excited electrons, in turn, can be captured by oxygen molecules adsorbed on the surface or “dissolved” in the zeolite lattice, producing active $\text{O}_2^{\cdot -}$ radical anions. At the same time, positively charged “holes” could be restored by water molecules, thus generating active radicals OH^\bullet [23].

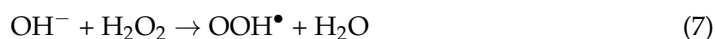
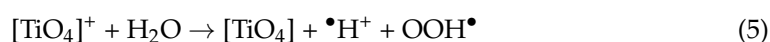
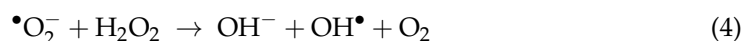


Previously, it was shown that both $\bullet\text{O}_2^-$, and OH^\bullet are involved in the oxidation of organic compounds, with the latter playing a dominant role [23,58–62]. However, because of the tendency of titanium dioxide to fast recombination of electron–hole pairs, on the one

hand [23,63], and the low content of titanium in the sample, on the other hand, the rate of oxidation of crystal violet in the absence of H_2O_2 was only $0.04\% \cdot \text{min}^{-1}$.

The addition of H_2O_2 leads to a sharp increase in the reaction rate even in the absence of a catalyst. The oxidation proceeds via radical mechanism. The introduction of a catalyst into the system contributes to a slight increase in the reaction rate, approximately equal to the rate in a system with a catalyst but without an oxidizer. At the same time, the shape of the kinetic curve changes: in the presence of a catalyst, the reaction rate does not depend on the concentration of the substrate. Two possible reaction paths in the presence of a titanium-containing catalyst should be noted here:

1. The role of Ti (IV) mainly consists of the acceleration of the H_2O_2 decomposition and the generation of OH^\bullet ; further oxidation of the substrate occurs via the radical mechanism in the light, as well as in the absence of a catalyst (Equations (4)–(9)):



2. Titanium directly interacts with both the oxidizing agent and the substrate, thus directing the reaction through a coordination mechanism similar to the epoxidation process. The advantage of this route is the reduced reaction rate at the initial stage compared to the catalyst-free system, where the reaction could proceed only via the radical mechanism. Indeed, in this case, only tetracoordinated titanium located on the surface can take part in the oxidation; it has vacancies in the coordination environment and, thus, it is capable of attaching hydrogen peroxide and substrate molecules to start the catalytic cycle. The concentration of tetracoordinated titanium is low and according to Raman and DRIFTS, the ^{29}Si NMR is 15–20%. Nevertheless, both mechanisms do not exclude each other and when the reaction proceeds in the presence of both TiO_2 / Al-ZSM-12 and H_2O_2 , it can be assumed that they coexist simultaneously. In this case, the possibility of the reaction proceeding via the coordination mechanism in the presence of H_2O_2 compensates for the tendency of the titanium oxide fragments in the zeolite structure to recombine the electron-hole pairs, which suppresses photocatalytic activity.

3. Materials and Methods

The synthesis of Al-ZSM-12 and TiO_2 / Al-ZSM-12 zeolites was carried out using the following reagents: a colloidal solution of silicon oxide LUDOX HS-40 [40 mass.%, Sigma-Aldrich, St. Louis, MO, USA], aluminum sulfate octadecahydrate $[\text{Al}_2(\text{SO}_4)_3 \cdot 18\text{H}_2\text{O}]$, Sigma-Aldrich, 99%, titanium isopropoxide $[\text{Ti}(\text{O}-i\text{-C}_3\text{H}_7)_4]$, Sigma-Aldrich, 97%, methyltriethylammonium chloride $[\text{CH}_3\text{N}(\text{C}_2\text{H}_5)_3\text{Cl}]$, Sigma-Aldrich, 97%, sodium hydroxide $[\text{NaOH}]$, Komponent-Reaktiv, Moscow, Russia, 98%, ammonium nitrate $[\text{NH}_4\text{NO}_3]$, Khimmed, Moscow, Russia, 98%, and crystal violet dye $[\text{C}_{25}\text{H}_{30}\text{N}_3\text{Cl}]$, Sigma-Aldrich, 98%.

3.1. Synthesis of Zeolites Al-ZSM-12 and TiO_2 / Al-ZSM-12

Solution A, consisting of 12.6 g of distilled water, 0.4 g of $\text{Al}_2(\text{SO}_4)_3 \cdot 18\text{H}_2\text{O}$, 1 g of NaOH , and 3.3 g of $[\text{MTEA}]\text{Cl}$ used as a template, was stirred until all of the components became completely dissolved. During the synthesis of zeolite TiO_2 / Al-ZSM-12 (molar ratio TiO_2 / $\text{Al}_2\text{O}_3 = 1$), 0.17 g of $\text{Ti}(\text{O}-i\text{-C}_3\text{H}_7)_4$ was added to solution A. Solution B, consisting of 25.2 g of a 40% (wt.) colloidal solution of silicon dioxide of the brand LUDOX HS-40 and 10.1 g of distilled water, was stirred until the reaction mixture was homogeneous. Solution A was dropped into solution B and stirred gently. The composition of reaction mixtures:

20.83Na₂O:1Al₂O₃:280SiO₂: 35.3 template:3501.6H₂O—for Al-ZSM-12
 20.83Na₂O:1Al₂O₃:1TiO₂:280SiO₂:35.3 template:3501.6H₂O—for TiO₂/Al-ZSM-12

The gel was poured into a Teflon liner and placed into the autoclave, which was heated at 155 °C for 120 h. The product was filtered off, washed with distilled water, dried at 110 °C, and then calcined at 550 °C for 10 h (heating rate 1 deg·min^{−1}).

To obtain the H-form of zeolites, the synthesized materials were treated 3 times with a 1 M aqueous solution of NH₄NO₃ at 80 °C for 17 h. Then, the solid product was filtered off, washed with distilled water, dried at 110 °C, and then calcined at 550 °C for 8 h (heating rate 1 deg·min^{−1}).

3.2. Characterization

The X-ray diffraction (XRD) analysis was performed with a Rigaku Rotaflex D/max-RC instrument (Rigaku, Tokyo, Japan) using copper K α radiation ($\lambda = 0.154$ nm). The diffraction pattern of the sample was recorded in the angular range $2\theta = 3\text{--}50^\circ$ with a range of 0.04° at the shooting rate of $2\text{ deg}\cdot\text{min}^{-1}$. The reflections corresponding to the crystalline and amorphous components were described using the pseudo-Voigt profile, which is a linear combination of the Lorentz and Gauss functions. The degree of crystallinity C_I was calculated using the MDI Jade 6.5 (<https://materialsdata.com/projtd.html>, accessed on 18 December 2022) program using the formula: $C_I = \frac{A_{CR}}{A_{SUM}}$, where A_{CR} is the sum of the integral intensities (areas) of reflections corresponding to the crystalline phase, A_{SUM} is the total area of all reflections that approximated the diffraction pattern. This method is used in the absence of standard samples, the crystallinity of which is taken as 100%.

N₂ adsorption–desorption isotherms were recorded with a Gemini VII 2390 (V1.02t) instrument (Micromeritics, Gemini, New York, NY, USA) at 77 K (−196 °C). Before the measurements, the samples were degassed at a temperature of 300 °C for 6 h. To calculate the surface area, the Brunauer–Emmett–Teller (BET) method was used based on adsorption data in the relative pressure range $p/p_0 = 0.05\text{--}0.2$. The total pore volume was determined from the amount of adsorbed nitrogen at a relative pressure $p/p_0 = 0.95$. The volume of micropores was determined using the t -plot method.

X-ray fluorescence elemental (XRF) analysis was conducted with the Thermo ARL Perform'x Sequential XFR instrument (Thermo Fisher Scientific, Waltham, MA, USA) using a 2500 W X-ray tube. Before the analysis, the samples weighing 200 mg were pressed into a tablet with boric acid.

Scanning electron microscopy (SEM). The micrographs of the samples were taken on a Hitachi (Chiyoda City, Tokyo) TM3030 desktop scanning electron microscope. The information on the local elemental composition and the distribution of elements on the sample surface was obtained using an energy dispersive spectrometer (EDX) with the Quantax 70 software and hardware system.

Transmission electron microscopy (TEM). The structure and surface morphology of the synthesized samples were studied using transmission electron microscopy on a LEO AB OMEGA instrument with the magnification from 80 to 500,000 and the image resolution of 0.2–0.34 nm.

Fourier Transform Infrared Spectroscopy (FTIR). The samples were analyzed via the Fourier transform IR spectroscopy method on a Nicolet IR2000 instrument (Thermo Scientific) through the multiple attenuated total internal reflection method using a Multireflection HATR attachment containing a 45° ZnSe crystal for various wavelength ranges with a resolution of 4 cm^{-1} .

Raman spectroscopy (Raman). Raman spectra were recorded on a Horiba LabRAM HR Evolution spectrometer. Raman spectra were excited using a He:Cd laser, $\lambda = 325$ nm. Spectral resolution 3 cm^{-1} .

UV–visible diffuse reflectance spectroscopy (DRS UV-Vis). Absorption spectra were recorded on a Lambda 950 spectrophotometer (Perkin Elmer, Waltham, MA, USA) in the wavelength range from 200 to 2500 nm in the diffuse reflection mode.

Diffuse reflectance infrared Fourier transform spectroscopy (DRIFTS). Diffuse reflectance IR spectra were obtained using a PIKE Diffus IR high-temperature cell (Madison, WI, USA) connected to a VERTEX-70 IR Fourier spectrometer (Bruker, Yokohama, Japan). The spectra were recorded in the range of 4000–500 cm^{-1} with the resolution of 40 cm^{-1} (100 scans/spectrum).

Photoluminescence spectroscopy (PL spectroscopy). PL spectra were obtained using a Fluoromax Horiba Tobin Yvon 55 V spectrofluorometer (Horiba, Kyoto, Japan). The spectra were recorded at room temperature and λ excitation = 250 nm.

Solid-State nuclear magnetic resonance spectroscopy (SS NMR) on different nuclei. NMR spectra with magic angle rotation were recorded on a Bruker AVANCE-II 400 WB spectrometer with the magnetic field of 9.4 T, which corresponds to operating frequencies ν (^1H) = 400.13 MHz, ν (^{27}Al) = 104.2 MHz, ν (^{29}Si) = 79.5 MHz, ν (^{23}Na) = 105.8 MHz, and H/X MAS WVT using a magic angle spinning (MAS) sensor. The diameter of the MAS-rotor is 4 mm, the rotation frequency is 12,000 Hz. The spectra were recorded using the single-pulse technique with the following parameters (Table 5):

Table 5. The conditions for the conduction of solid-state NMR spectroscopy.

Nucleus	Rotation Angle, °	Pulse Duration, μs	Number of Scans	Interval between Scans, s	External Standard (0 ppm)
^1H	90	2.9	16	3	NH_4OH , 25% aqueous solution
^{27}Al	15	0.8	1024	0.5	$\text{Al}(\text{NO}_3)_3$, 1M aqueous solution
^{29}Si	90	4	256	60	$\text{Si}(\text{CH}_3)_4$
^{23}Na	30	2	1	2048	NaCl , 1M aqueous solution

For the spectra of ^{29}Si , the technique with polarization transfer (CP/MAS) from ^1H to ^{29}Si (contact time, 4 ms; number of scans, 2048; the interval between scans—2.5 s) was also used.

Thermogravimetric (TG), differential scanning calorimetry (DSC) and differential thermal analysis (DTA). TG/DSC/DTA was performed on a TG/DSC1 Mettler Toledo instrument. The sample placed in a 150 μL Al_2O_3 crucible was heated at the constant rate of 10 $\text{deg}\cdot\text{min}^{-1}$ in the range of 1000 $^\circ\text{C}$ in the air flow (70 $\text{mL}\cdot\text{min}^{-1}$).

Temperature-programmed ammonia desorption (NH_3 -TPD). The acidity of the samples was determined on a Micromeritics AutoChem HP2950 instrument. The test sample with the fraction of 0.25–1 mm and the mass of 0.15–0.2 g was placed in the quartz reactor, after which it was blown in the helium flow at 500 $^\circ\text{C}$ for 60 min, then saturated with ammonia in the ammonia/nitrogen mixture (10 vol. % ammonia) for 30 min at 60 $^\circ\text{C}$. Excess ammonia was purged with helium at 100 $^\circ\text{C}$ for 60 min at the flow rate of 30 $\text{mL}\cdot\text{min}^{-1}$. Then, the sample was analyzed in the helium flow in the temperature range from 100 to 800 $^\circ\text{C}$ at the heating rate of 8 $\text{deg}\cdot\text{min}^{-1}$. Desorbed ammonia was recorded using a thermal conductivity detector.

Fourier Transform Infrared Spectroscopy of adsorbed pyridine (FTIR-Py), 2,6-di-tert-butyl-pyridine at external surface (FTIR-2,6-dTBP), deuterated acetonitrile (FTIR- CD_3CN). IR spectra were recorded on a Nicolet Protégé 460 instrument with the optical resolution of 4 cm^{-1} and the range of 4000–400 cm^{-1} . Disk-shaped samples ($D = 1.6\text{-cm}$, $\rho \sim 10\text{ mg}\cdot\text{cm}^{-2}$) were activated in an IR cell at 400 $^\circ\text{C}$ at the heating rate of 7.5 $\text{deg}\cdot\text{min}^{-1}$ for 2 h and the pressure of 10^{-5} Torr. The adsorption of probe molecules was carried out for 30 min at 150 $^\circ\text{C}$ and the pressure of 2 Torr for pyridine and 2,6-di-tert-butylpyridine, and 0.5 Torr for acetonitrile. At the end of the adsorption cycle, pyridine was desorbed at 150 $^\circ\text{C}$ for 15 min.

The concentrations of BASs (Brønsted acid sites) and LASs (Lewis acid sites) were determined on the intensity of adsorbed pyridine bands (1545 and 1450 cm^{-1} , respectively); extinction coefficients were used in the calculations using the FTIR-Py method.

To determine the Brønsted acid sites on the outer surface of the zeolite, a 1620 cm^{-1} band of adsorbed 2,6-di-*tert*-butyl-pyridine was used via the FTIR-2,6-dTBP method.

The determination of the titanium state in zeolites was carried out using the FTIR- CD_3CN method.

Investigation of acidity using Diffuse Reflectance Infrared Fourier Transform Spectroscopy (DRIFTS-acid). The sample powder was placed in a special crucible in the PIKE Diffus IR high-temperature cell coupled to a Bruker VERTEX-70 IR Fourier spectrometer. The catalyst was calcined in the argon flow in the temperature range of $25\text{--}450\text{ }^\circ\text{C}$; it was cooled to room temperature in the argon flow. The relative intensities of the bands in the spectra of zeolites recorded in the argon flow at $450\text{ }^\circ\text{C}$ were used to determine the percentage composition of weak, medium, and strong Brønsted acid sites. The 1875 cm^{-1} band was used as an internal standard. This band is the overtone of the 990 cm^{-1} band from the Si–O frame bonds and its intensity does not depend on temperature.

3.3. The Technique of the Catalytic Experiments

The catalytic activity of the synthesized zeolite was studied in the reaction of photodegradation of crystal violet in the aqueous medium. This study included the following steps:

1. Suspension preparation. 2 mL of water was added to a 1.5 mg weighed portion of the test sample, after which stirring was carried out for 30 min until a homogeneous suspension was formed;
2. Dye adsorption on the surface of the photocatalyst. The aqueous solution of crystal violet dye ($40\text{ }\mu\text{L}$, $400\text{ mg}\cdot\text{L}^{-1}$) was added to the resulting suspension. The suspension was vigorously stirred in the darkness for 45 min to establish the adsorption–desorption equilibrium and prevent premature photocatalytic decomposition of the dye in the light. Then, hydrogen peroxide ($40\text{ }\mu\text{L}$, 3% solution) was added to the suspension, if necessary;
3. Photocatalytic activity measurement. After the adsorption–desorption equilibrium was established, the zeolite suspension was irradiated with an Ocean Optics HPX-2000 xenon lamp (the radiation power of 1.52 mW , measured in the range of $200\text{--}1100\text{ nm}$ with an integrated optical power meter). The spectrophotometric analysis of the suspension was performed using an Ocean Optics QE65000 spectrophotometer. The dye concentration was calculated from the optical density at the absorption maximum ($\lambda\sim 590\text{ nm}$) minus the background absorption ($\lambda = 700\text{ nm}$) of the spectrum of the catalyst suspension without the dye. The control experiment on the decomposition of the dye using hydrogen peroxide in the light was carried out in the absence of a catalyst.

4. Conclusions

In this study, $\text{aTiO}_2/\text{Al-ZSM-12}$ zeolite was synthesized using the hydrothermal method. Its textural, structural, morphological, and acid properties were studied in detail. Using X-ray phase analysis and IR spectroscopy, it was established that the obtained samples belonged to the MTW structural type. It was shown that the introduction of titanium in the molar ratio $\text{Ti}/\text{Al} = 1:1$ led to significant changes in the structure of the zeolite. Using the nitrogen adsorption method, it was shown that adsorption–desorption isotherms belonged to type I, characteristic of microporous zeolites, with an H4 hysteresis loop. During the hydrothermal synthesis, titanium ions which were present in the material in the form of TiO_4^{2-} anions acted as an inhibitor, slowing down the growth of crystallites along the *a* and *c* axes. The impurities $\text{Al}_2\text{O}_3\cdot\text{TiO}_2$, $\text{Na}_2\text{O}\cdot\text{TiO}_2$, Silica-X were formed as by-products and led to a decrease in the surface area (from 274 to $266\text{ cm}^3/\text{g}$). A decrease in the degree of crystallinity (from 93% to 83%) was affected by the incomplete incorporation

of silicon dioxide into the framework zeolite. The presence of tetrahedral titanium in the $\text{TiO}_2/\text{Al-ZSM-12}$ sample was confirmed by bands with maxima at 517 cm^{-1} (Raman) and 953 cm^{-1} (DRIFTS), the appearance of octahedral titanium was confirmed by a band with the maximum at 695 cm^{-1} (Raman), a small shoulder in the DRS UV-Vis spectrum in the region of 250–310 nm indicated the presence of penta- and octa-coordinated titanium, and the formation of TiO_2 clusters. The PL analysis data of the $\text{TiO}_2/\text{Al-ZSM-12}$ zeolite (wavelengths with maxima at 600–700 nm) characterized the presence of OH groups and H_2O molecules in the environment of titanium, which corresponded to the absorption band maximum at 695 cm^{-1} (Raman).

The presence of tetrahedral aluminum in the structure of both zeolites was confirmed by the ^{27}Al NMR spectra (the chemical shift at 55.6 ppm); the presence of the octahedral aluminum is typical for the zeolite Al-ZSM-12 (a chemical shift of about 0 ppm). The ^1H NMR spectra contained isolated Si–OH groups located on the outer surface of both zeolites (1.1–1.8 ppm); internal Al–OH groups (2.8 ppm); fragments of Si–O(H)–Al forming Brønsted acid sites (3.8, 4.0, and 4.2 ppm); hydroxyls associated with Si–OH \cdots O–hydrogen bonds (7.1 and 7.7 ppm). A similar shift for the $\text{TiO}_2/\text{Al-ZSM-12}$ sample at 4 ppm indicated a lower concentration of Brønsted acid sites. According solid ^{29}Si and ^1H - ^{29}Si CP/MAS NMR, the two allowed chemical shifts (at -112.5 and -102.5 ppm) corresponding to the Q^4 and Q^3 tetrahedral fragments appearing from the formation of silanol groups on the zeolite surface. In the ^1H - ^{29}Si CP/MAS NMR spectra of both samples, a chemical shift was observed at -92 ppm suggesting that the samples contained a $[\text{Si}(\text{OSi})_2(\text{OAl})_1(\text{OTi})_1]$ particle of the Q^2 type. According the ^{23}Na NMR spectrum, the chemical shift at -9.2 ppm in the of the $\text{TiO}_2/\text{Al-ZSM-12}$ zeolite was more intense due to its higher content of sodium, which corresponded to a lower degree of crystallinity compared to the Al-ZSM-12 zeolite.

According thermogravimetric, differential scanning calorimetry, and differential thermal analysis, a gradual decrease in weight loss in the Al-ZSM-12 sample (in the temperature range of 130–1000 °C, 2.8%) was associated with the destruction of the hydrogen bonds and dehydroxylation of the surface Si–OH and Al–OH groups. A more intense dehydroxylation in the case of the $\text{TiO}_2/\text{Al-ZSM-12}$ zeolite (4.8%) indicated a strong interaction of titanium with the OH groups.

Using NH_3 -TPD and IR spectroscopy of the adsorbed pyridine, 2,6-di-tert-butylpyridine, deuterated acetonitrile and DRIFTS-acid, the predominant content of weak acid sites in the $\text{TiO}_2/\text{Al-ZSM-12}$ sample was established, with Lewis acid sites predominating.

The NH_3 -TPD data showed that the $\text{TiO}_2/\text{Al-ZSM-12}$ sample, compared to Al-ZSM-12, was characterized by a higher concentration of weak acid sites (ammonia adsorption at 100–300 °C) formed by Si–O–Ti fragments and Si–O–Al, and the reduced concentration of strong acid sites (ammonia desorption at 300–550 °C) may be caused by incomplete H^+/Na^+ ion exchange inside the 12-membered ring channels.

In the $\text{TiO}_2/\text{Al-ZSM-12}$ zeolite (FTIR-pyridine, 2,6-di-tert-butylpyridine), the intensity of the bands of the silanol and Al–OH groups was inferior to that of the Al-ZSM-12 zeolite due to the isomorphic substitution of aluminum by titanium. Pyridine bonded to the OH groups on the surface of the titanium clusters was identified by a band with the absorption maximum at 1575 cm^{-1} (corresponds to Lewis acid sites). In the $\text{TiO}_2/\text{Al-ZSM-12}$ zeolite, the band with the absorption maximum at 1446 cm^{-1} was supposed to indicate an insignificant proportion of tetrahedral titanium.

According to the adsorption spectra of deuterated acetonitrile, the Lewis and Brønsted acid sites were determined in the zeolites Al-ZSM-12 and $\text{TiO}_2/\text{Al-ZSM-12}$, which appeared on titanium and aluminum. The concentration of weak Lewis acid sites was determined from the bands with the absorption maximum at 2306 cm^{-1} (Al-ZSM-12) formed by Al^{+3} and at 2300 cm^{-1} ($\text{TiO}_2/\text{Al-ZSM-12}$) formed by Ti^{+4} . According to DRIFTS-acid, the band with the absorption maximum at $3560\text{--}3500\text{ cm}^{-1}$ in the spectrum of the $\text{TiO}_2/\text{Al-ZSM-12}$ zeolite broadened at the association with H_2O . O–H stretch vibrations in the composition of the hydronium cation (H_3O^+) produced bands with the absorption maximum below 3300 cm^{-1} . The DRIFTS-acid data supported the conclusion that the introduction of

titanium led a to the redistribution of the number of Brønsted acid sites between the weak and medium sites.

The synthesized $\text{TiO}_2/\text{Al-ZSM-12}$ zeolite showed activity in the photocatalytic oxidation of the crystal violet dye in the presence of H_2O_2 as an oxidizing agent. In this case, the activity of the $[\text{TiO}_2/\text{Al-ZSM-12} + \text{H}_2\text{O}_2]$ system exceeded the activity of the systems containing only zeolite or only H_2O_2 . It was assumed that in the presence of the $[\text{TiO}_2/\text{Al-ZSM-12} + \text{H}_2\text{O}_2]$ system, the reaction proceeded simultaneously via the radical mechanism with photoinduced generation of OH^\bullet radicals and the coordination mechanism.

The possibility of isomorphic substitution of aluminum by titanium in Al-ZSM-12 zeolite in the $\text{TiO}_2/\text{Al}_2\text{O}_3 = 1:1$ molar ratio was shown. Due to this, the concentration of Lewis acid sites increased in the resulting zeolite. It is assumed that materials of this type, exhibiting a higher Lewis acidity, can promote the isomerization reactions of *n*-alkanes and aromatic hydrocarbons.

Author Contributions: Conceptualization, L.A.K.; methodology, D.E.T.; validation, D.E.T. and V.A.O.; formal analysis, L.A.K. and E.R.N.; investigation, D.E.T. and A.A.S.; resources, E.R.N. and A.A.S.; data curation, V.A.O.; writing—original draft preparation, D.E.T. and M.D.K.; writing—review and editing, A.V.Z., Z.L. and K.W.; visualization, V.A.O.; supervision, A.L.M.; project administration, A.L.M.; funding acquisition, S.V.E. All authors have read and agreed to the published version of the manuscript.

Funding: The study is financially supported by the Ministry of Science and Higher Education of the Russian Federation (Agreement No. 075-15-2021-1363).

Acknowledgments: The work was carried out using the equipment from the Center for Collective Use “Analytical Center for Problems of Deep Oil Refining and Petrochemistry” TIPS RAS (A.V. Topchiev Institute of Petrochemical Synthesis, Russian Academy of Sciences).

Conflicts of Interest: The authors declare no conflict of interest requiring disclosure in this article.

References

1. Ramsay, J.D.F.; Kallus, S. Zeolite Membranes. *Membr. Sci. Technol.* **2000**, *6*, 373–395.
2. Zeolite Catalysts Come into Focus. *Nat. Mater.* **2020**, *19*, 1037. [[CrossRef](#)] [[PubMed](#)]
3. Naranov, E.R.; Dement'ev, K.I.; Gerzeliev, I.M.; Kolesnichenko, N.V.; Roldugina, E.A.; Maksimov, A.L. The Role of Zeolite Catalysis in Modern Petroleum Refining: Contribution from Domestic Technologies. *Pet. Chem.* **2019**, *59*, 247–261. [[CrossRef](#)]
4. Naranov, E.R.; Golubev, O.V.; Guseva, A.I.; Nikulshin, P.A.; Maksimov, A.L.; Karakhanov, E.A. Hydrotreating of Middle-Distillate Fraction on Sulfide Catalysts Containing Crystalline Porous Aluminosilicates. *Pet. Chem. Neft.* **2017**, *57*, 965–5441. [[CrossRef](#)]
5. Fairuzov, D.; Gerzeliev, I.; Maximov, A.; Naranov, E. Catalytic Dehydrogenation of Ethane: A Mini Review of Recent Advances and Perspective of Chemical Looping Technology. *Catalysts* **2021**, *11*, 833. [[CrossRef](#)]
6. Shavaleev, D.A.; Pavlov, M.L.; Basimova, R.A.; Sadovnikov, A.A.; Sudin, V.V.; Smirnova, E.M.; Demikhova, N.R.; Grigor'ev, Y.V.; Maksimov, A.L.; Naranov, E.R. Synthesis of Modified Catalyst for Liquid Phase Alkylation of Benzene with Ethylene. *Pet. Chem.* **2020**, *60*, 1073–1079. [[CrossRef](#)]
7. Sadovnikov, A.A.; Arapova, O.V.; Russo, V.; Maximov, A.L.; Murzin, D.Y. Synergy of Acidity and Morphology of Micro-/Mesoporous Materials in the Solid-Acid Alkylation of Toluene with 1-Decene. *Ind. Eng. Chem. Res.* **2022**, *61*, 1994–2009. [[CrossRef](#)]
8. Bok, T.O.; Andriako, E.P.; Ivanova, I.I. Effect of Binder Content on the Properties of Nanocrystalline Zeolite BEA-Based Catalysts for Benzene Alkylation with Propylene. *Pet. Chem.* **2021**, *61*, 901–907. [[CrossRef](#)]
9. Saab, R.; Polychronopoulou, K.; Anjum, D.H.; Charisiou, N.D.; Goula, M.A.; Hinder, S.J.; Baker, M.A.; Schiffer, A. Effect of $\text{SiO}_2/\text{Al}_2\text{O}_3$ Ratio in Ni/Z-zeolite-Y and Ni-W/Z-zeolite-Y Catalysts on Hydrocracking of Heptane. *Mol. Catal.* **2022**, *528*, 112484. [[CrossRef](#)]
10. Liu, B.; Zhang, J.; Huang, Y.; Xiong, F.; Luo, R. Defect-Designed ZSM-12 Zeolites for Alkylation of Phenol with Tert-butyl Alcohol. *Mol. Catal.* **2022**, *519*, 112144. [[CrossRef](#)]
11. Tsai, S.-T.; Chao, P.-H.; Liu, S.-B.; Tsai, T.-C. Synergism of Acidic Zeolite and Pt/Z-zeolite in Aromatics Transalkylation. In *Studies in Surface Science and Catalysis*; Elsevier: Amsterdam, The Netherlands, 2008; pp. 1183–1186.
12. Lu, X.; Guo, Y.; Zhang, Y.; Ma, R.; Fu, Y.; Zhu, W. Enhanced Catalytic Activity of Pt/H-ZSM-12 via Alkaline Post-Treatment for the Hydroisomerization of *n*-Hexane. *Microporous Mesoporous Mater.* **2020**, *306*, 110459. [[CrossRef](#)]
13. Carvalho, K.T.G.; Urquieta-Gonzalez, E.A. Microporous–Mesoporous ZSM-12 Zeolites: Synthesis by Using a Soft Template and Textural, Acid and Catalytic Properties. *Catal. Today* **2015**, *243*, 92–102. [[CrossRef](#)]

14. Sanhoob, M.A.; Muraza, O.; Yoshioka, M.; Qamaruddin, M.; Yokoi, T. Lanthanum, Cerium, and Boron Incorporated ZSM-12 Zeolites for Catalytic Cracking of *n*-Hexane. *J. Anal. Appl. Pyrolysis* **2018**, *129*, 231–240. [\[CrossRef\]](#)
15. Tsaplin, D.E.; Makeeva, D.A.; Kulikov, L.A.; Maksimov, A.L.; Karakhanov, E.A. Synthesis of ZSM-12 Zeolites with New Templates Based on Salts of Ethanolamines. *Russ. J. Appl. Chem.* **2018**, *91*, 1957–1962. [\[CrossRef\]](#)
16. Jia, X.; Zhang, Y.; Gong, Z.; Wang, B.; Zhu, Z.; Jiang, J.; Xu, H.; Sun, H.; Han, L.; Wu, P.; et al. Bolaform Molecules Directing Intergrown Zeolites. *J. Phys. Chem. C* **2018**, *122*, 9117–9126. [\[CrossRef\]](#)
17. Mal, N.K.; Bhaumik, A.; Kumar, R.; Ramaswamy, A.V. Sn-ZSM-12, a New, Large Pore MTW Type Tin-Silicate Molecular Sieve: Synthesis, Characterization and Catalytic Properties in Oxidation Reactions. *Catal. Lett.* **1995**, *33*, 387–394. [\[CrossRef\]](#)
18. Zhi, Y.-X.; Tuel, A.; Taarit, Y.B.; Naccache, C. Synthesis of Gallosilicates—MTW-Type Structure Zeolites: Evidence of Ga-Substituted T Atoms. *Zeolites* **1992**, *12*, 138–141. [\[CrossRef\]](#)
19. Reddy, K.M.; Moudrakovski, I.; Sayari, A. VS-12: A Novel Large-Pore Vanadium Silicate with ZSM-12 Structure. *J. Chem. Soc. Chem. Commun.* **1994**, 1491–1492. [\[CrossRef\]](#)
20. Tuel, A. Synthesis, Characterization, and Catalytic Properties of the New TiZSM-12 Zeolite. *Zeolites* **1995**, *15*, 236–242. [\[CrossRef\]](#)
21. Davis, R.J.; Liu, Z. Titania–Silica: A Model Binary Oxide Catalyst System. *Chem. Mater.* **1997**, *9*, 2311–2324. [\[CrossRef\]](#)
22. Noguera, C. Chapter 2 Clean Oxide Surfaces: A Theoretical Review. *Chem. Phys. Solid Surf.* **2001**, *9*, 35–93.
23. Ullah, R.; Liu, C.; Panezai, H.; Gul, A.; Sun, J.; Wu, X. Controlled Crystal Phase and Particle Size of Loaded-TiO₂ Using Clinoptilolite as Support via Hydrothermal Method for Degradation of Crystal Violet Dye in Aqueous Solution. *Arab. J. Chem.* **2020**, *13*, 4092–4101. [\[CrossRef\]](#)
24. Djellabi, R.; Giannantonio, R.; Falletta, E.; Bianchi, C.L. SWOT Analysis of Photocatalytic Materials towards Large Scale Environmental Remediation. *Curr. Opin. Chem. Eng.* **2021**, *33*, 100696. [\[CrossRef\]](#)
25. Mesbah, M.; Sarraf, M.; Dabbagh, A.; Nasiri-Tabrizi, B.; Paria, S.; Banihashemian, S.M.; Bushroa, A.R.; Faraji, G.; Tsuzuki, T.; Madaah Hosseini, H.R. Synergistic Enhancement of Photocatalytic Antibacterial Effects in High-Strength Aluminum/TiO₂ Nanoarchitectures. *Ceram. Int.* **2020**, *46*, 24267–24280. [\[CrossRef\]](#)
26. Prado, R.; Erdocia, X.; Labidi, J. Effect of the Photocatalytic Activity of TiO₂ on Lignin Depolymerization. *Chemosphere* **2013**, *91*, 1355–1361. [\[CrossRef\]](#)
27. Aboagye, D.; Medina, F.; Contreras, S. Toward a Facile Depolymerization of Alkaline Lignin into High-Value Platform Chemicals via the Synergetic Combination of Mechanocatalysis with Photocatalysis or Fenton Process. *Catal. Today*, **2022**; in press. [\[CrossRef\]](#)
28. Machut, C.; Kania, N.; Léger, B.; Wyrwalski, F.; Noël, S.; Addad, A.; Monflier, E.; Ponchel, A. Fast Microwave Synthesis of Gold-Doped TiO₂ Assisted by Modified Cyclodextrins for Photocatalytic Degradation of Dye and Hydrogen Production. *Catalysts* **2020**, *10*, 801. [\[CrossRef\]](#)
29. Torres, J.C.; Cardoso, D. The Influence of Gel Alkalinity in the Synthesis and Physicochemical Properties of the Zeolite [Ti,Al]-Beta. *Microporous Mesoporous Mater.* **2008**, *113*, 204–211. [\[CrossRef\]](#)
30. Subagyo, R.; Tehubijuluw, H.; Utomo, W.P.; Rizqi, H.D.; Kusumawati, Y.; Bahruji, H.; Prasetyoko, D. Converting Red Mud Wastes into Mesoporous ZSM-5 Decorated with TiO₂ as an Eco-Friendly and Efficient Adsorbent-Photocatalyst for Dyes Removal. *Arab. J. Chem.* **2022**, *15*, 103754. [\[CrossRef\]](#)
31. Huang, F.; Hao, H.; Sheng, W.; Dong, X.; Lang, X. Cooperative Photocatalysis of Dye–Ti-MCM-41 with Trimethylamine for Selective Aerobic Oxidation of Sulfides Illuminated by Blue Light. *J. Colloid Interface Sci.* **2023**, *630*, 921–930. [\[CrossRef\]](#)
32. Kulikov, L.A.; Tsaplin, D.E.; Knyazeva, M.I.; Levin, I.S.; Kardashev, S.V.; Filippova, T.Y.; Maksimov, A.L.; Karakhanov, E.A. Effect of Template Structure on the Zeolite ZSM-12 Crystallization Process Characteristics. *Pet. Chem.* **2019**, *59*, S60–S65. [\[CrossRef\]](#)
33. Kamimura, Y.; Iyoki, K.; Elangovan, S.P.; Itabashi, K.; Shimojima, A.; Okubo, T. OSDA-Free Synthesis of MTW-Type Zeolite from Sodium Aluminosilicate Gels with Zeolite Beta Seeds. *Microporous Mesoporous Mater.* **2012**, *163*, 282–290. [\[CrossRef\]](#)
34. Akyalcin, S.; Akyalcin, L.; Bjørgen, M. Optimization of Desilication Parameters of Low-Silica ZSM-12 by Taguchi Method. *Microporous Mesoporous Mater.* **2019**, *273*, 256–264. [\[CrossRef\]](#)
35. Ogura, M.; Nakata, S.; Kikuchi, E.; Matsukata, M. Effect of NH₄⁺ Exchange on Hydrophobicity and Catalytic Properties of Al-Free Ti–Si–Beta Zeolite. *J. Catal.* **2001**, *199*, 41–47. [\[CrossRef\]](#)
36. Gomez, S.; Marchena, C.L.; Pizzio, L.; Pierella, L. Preparation and Characterization of TiO₂/HZSM-11 Zeolite for Photodegradation of Dichlorvos in Aqueous Solution. *J. Hazard. Mater.* **2013**, *258*, 19–26. [\[CrossRef\]](#)
37. Reddy, J.S.; Kumar, R.; Csicsery, S.M. Synthesis, Characterization, and Catalytic Properties of Metallo-Titanium Silicate Molecular Sieves with MEL Topology. *J. Catal.* **1994**, *145*, 73–78. [\[CrossRef\]](#)
38. Zhu, H.-B.; Xia, Q.-H.; Guo, X.-T.; Su, K.-X.; Hu, D.; Ma, X.; Zeng, D.; Deng, F. Synthesis and Structure-Directing Effect of Piperazinium Hydroxides Derived from Piperazines for the Formation of Porous Zeolites. *Mater. Lett.* **2006**, *60*, 2161–2166. [\[CrossRef\]](#)
39. Wu, W.; Wu, W.; Kikhtyanin, O.V.; Li, L.; Toktarev, A.V.; Ayupov, A.B.; Khabibulin, J.F.; Echevsky, G.V.; Huang, J. Methylation of Naphthalene on MTW-Type Zeolites. Influence of Template Origin and Substitution of Al by Ga. *Appl. Catal. A Gen.* **2010**, *375*, 279–288. [\[CrossRef\]](#)
40. Yang, J.; Zhang, J.; Zhu, L.; Chen, S.; Zhang, Y.; Tang, Y.; Zhu, Y.; Li, Y. Synthesis of Nano Titania Particles Embedded in Mesoporous SBA-15: Characterization and Photocatalytic Activity. *J. Hazard. Mater.* **2006**, *137*, 952–958. [\[CrossRef\]](#)

41. Domoroshchina, E.; Kravchenko, G.; Kuz'micheva, G.; Markova, E.; Zhukova, A.; Pirutko, L.; Khramov, E.; Dorokhov, A.; Koroleva, A. The Role of the Compositions of HZSM-5 Zeolites Modified with Nanosized Anatase in Propane and Ethanol Conversion. *Catal. Today* **2022**, *397*, 511–525. [\[CrossRef\]](#)
42. Guo, Q.; Sun, K.; Feng, Z.; Li, G.; Guo, M.; Fan, F.; Li, C. A Thorough Investigation of the Active Titanium Species in TS-1 Zeolite by In Situ UV Resonance Raman Spectroscopy. *Chem.—Eur. J.* **2012**, *18*, 13854–13860. [\[CrossRef\]](#) [\[PubMed\]](#)
43. Xiong, G.; Cao, Y.; Guo, Z.; Jia, Q.; Tian, F.; Liu, L. The Roles of Different Titanium Species in TS-1 Zeolite in Propylene Epoxidation Studied by in Situ UV Raman Spectroscopy. *Phys. Chem. Chem. Phys.* **2016**, *18*, 190–196. [\[CrossRef\]](#)
44. Halasz, I.; Agarwal, M.; Senderov, E.; Marcus, B. Efficient Oxyfunctionalization of N-Hexane by Aqueous H₂O₂ over a New TS-PQTM Catalyst. *Catal. Today* **2003**, *81*, 227–245. [\[CrossRef\]](#)
45. Yamamoto, K.; Borjas García, S.E.; Muramatsu, A. Zeolite Synthesis Using Mechanochemical Reaction. *Microporous Mesoporous Mater.* **2007**, *101*, 90–96. [\[CrossRef\]](#)
46. Horikawa, H.; Iida, T.; Osga, R.; Ohara, K.; Kondo, J.N.; Wakihara, T. Crystallization of Ti-Rich *BEA Zeolites by the Combined Strategy of Using Ti–Si Mixed Oxide Composites and Intentional Aluminum Addition/Post-Synthesis Dealumination. *Cryst. Growth Des.* **2018**, *18*, 2180–2188. [\[CrossRef\]](#)
47. Wu, Z.Y.; Tao, Y.F.; Lin, Z.; Liu, L.; Fan, X.X.; Wang, Y. Hydrothermal Synthesis and Morphological Evolution of Mesoporous Titania–Silica. *J. Phys. Chem. C* **2009**, *113*, 20335–20348. [\[CrossRef\]](#)
48. Trong On, D.; Nguyen, S.; Hulea, V.; Dumitriu, E.; Kaliaguine, S. Mono- and Bifunctional MFI, BEA and MCM-41 Titanium-Molecular Sieves. Part 1. Synthesis and Characterization. *Microporous Mesoporous Mater.* **2003**, *57*, 169–180. [\[CrossRef\]](#)
49. Carati, A.; Flego, C.; Previde Massara, E.; Millini, R.; Carluccio, L.; Parker, W.; Bellussi, G. Stability of Ti in MFI and Beta Structures: A Comparative Study. *Microporous Mesoporous Mater.* **1999**, *30*, 137–144. [\[CrossRef\]](#)
50. Mazaj, M.; Zabukovec Logar, N.; Mali, G.; Novak Tušar, N.; Arčon, I.; Ristić, A.; Rečnik, A.; Kaučič, V. Synthesis and Structural Properties of Titanium Containing Microporous/Mesoporous Silicate Composite (Ti, Al)-Beta/MCM-48. *Microporous Mesoporous Mater.* **2007**, *99*, 3–13. [\[CrossRef\]](#)
51. Ovejero, G.; Van Grieken, R.; Uguina, M.A.; Serrano, D.P.; Melero, J.A. Bifunctional Properties of Al-TS-1 Synthesized by Wetness Impregnation of Amorphous Al₂O₃-TiO₂-SiO₂ Solids Prepared by the Sol-Gel Method. *Catal. Lett.* **1996**, *41*, 69–78. [\[CrossRef\]](#)
52. Ganapathy, S.; Gore, K.; Kumar, R.; Amoureux, J.-P. Multinuclear (27Al, 29Si, 47,49Ti) Solid-State NMR of Titanium Substituted Zeolite USY. *Solid State Nucl. Magn. Reson.* **2003**, *24*, 184–195. [\[CrossRef\]](#) [\[PubMed\]](#)
53. Kim, Y.; Kirkpatrick, R.J. High-Temperature Multi-Nuclear NMR Investigation of Analcime. *Am. Mineral.* **1998**, *83*, 339–347. [\[CrossRef\]](#)
54. García-Benjume, M.L.; Espitia-Cabrera, M.I.; Contreras-García, M.E. Hierarchical Macro-Mesoporous Structures in the System TiO₂-Al₂O₃, Obtained by Hydrothermal Synthesis Using Tween-20® as a Directing Agent. *Mater. Charact.* **2009**, *60*, 1482–1488. [\[CrossRef\]](#)
55. Nakabayashi, H. Properties of Acid Sites on TiO₂-SiO₂ and TiO₂-Al₂O₃ Mixed Oxides Measured by Infrared Spectroscopy. *Bull. Chem. Soc. Jpn.* **1992**, *65*, 914–916. [\[CrossRef\]](#)
56. Kurmach, M.M.; Yaremov, P.S.; Skoryk, M.O.; Shvets, O.V. Effect of Introduction of B³⁺ or Al³⁺ Ions in the Structure of Ti-, Sn-, AND Zr-Containing Hierarchical Zeolites on the Concentration of Lewis and Brønsted Acid Centers. *Theor. Exp. Chem.* **2016**, *52*, 190–196. [\[CrossRef\]](#)
57. Naranov, E.R.; Sadovnikov, A.A.; Bugaev, A.L.; Shavaleev, D.A.; Maximov, A.L. A Stepwise Fabrication of MFI Nanosheets in Accelerated Mode. *Catal. Today* **2021**, *378*, 149–157. [\[CrossRef\]](#)
58. Panahian, Y.; Arsalani, N.; Nasiri, R. Enhanced Photo and Sono-Photo Degradation of Crystal Violet Dye in Aqueous Solution by 3D Flower like F-TiO₂(B)/Fullerene under Visible Light. *J. Photochem. Photobiol. A Chem.* **2018**, *365*, 45–51. [\[CrossRef\]](#)
59. Pelaez, M.; Nolan, N.T.; Pillai, S.C.; Seery, M.K.; Falaras, P.; Kontos, A.G.; Dunlop, P.S.M.; Hamilton, J.W.J.; Byrne, J.A.; O'Shea, K.; et al. A Review on the Visible Light Active Titanium Dioxide Photocatalysts for Environmental Applications. *Appl. Catal. B Environ.* **2012**, *125*, 331–349. [\[CrossRef\]](#)
60. Cao, Y.; Li, X.; Bian, Z.; Fuhr, A.; Zhang, D.; Zhu, J. Highly Photocatalytic Activity of Brookite/Rutile TiO₂ Nanocrystals with Semi-Embedded Structure. *Appl. Catal. B Environ.* **2016**, *180*, 551–558. [\[CrossRef\]](#)
61. Banerjee, S.; Pillai, S.C.; Falaras, P.; O'Shea, K.E.; Byrne, J.A.; Dionysiou, D.D. New Insights into the Mechanism of Visible Light Photocatalysis. *J. Phys. Chem. Lett.* **2014**, *5*, 2543–2554. [\[CrossRef\]](#)
62. Pang, Y.; Xu, G.; Feng, Q.; Lv, J.; Qin, Y.; Zhang, Y.; Zheng, Z.; Wu, Y. Crystalline Orientation Preference for TiO₂ Nanotube Arrays with Efficient Photoelectrochemical Properties. *Phys. Lett. A* **2018**, *382*, 2759–2762. [\[CrossRef\]](#)
63. Derikvandi, H.; Nezamzadeh-Ejhi, A. Increased Photocatalytic Activity of NiO and ZnO in Photodegradation of a Model Drug Aqueous Solution: Effect of Coupling, Supporting, Particles Size and Calcination Temperature. *J. Hazard. Mater.* **2017**, *321*, 629–638. [\[CrossRef\]](#) [\[PubMed\]](#)

Disclaimer/Publisher's Note: The statements, opinions and data contained in all publications are solely those of the individual author(s) and contributor(s) and not of MDPI and/or the editor(s). MDPI and/or the editor(s) disclaim responsibility for any injury to people or property resulting from any ideas, methods, instructions or products referred to in the content.